

# Kinetics and Grain Boundary Selectivity of Discontinuous Precipitation in Binary Ni-Cr Alloy



N. KESKAR, A.K. PATTANAIK, K.V. MANI KRISHNA, D. SRIVASTAVA,  
and G.K. DEY

A supersaturated Ni-Cr alloy (42 wt pct Cr) was subjected to a series of aging heat treatments in the two-phase region in the temperature range of 923 K to 1123 K (650 °C to 850 °C) for different time periods. The resultant microstructures were seen to be composed of varying volume fractions of continuous (CP) and discontinuous precipitation (DP). The DP dominated at lower temperatures, while CP dominated at higher temperatures and the expected DP termination temperature was estimated to be 1138 K (865 °C). The kinetics of DP followed the Turnbull model at lower temperatures and the Aaronson–Liu model at higher temperatures. The nucleation and growth of DP cells, which occurred *via* the ‘precipitate driven grain boundary migration,’ was seen to be a strong function of the nature of the participating grain boundaries.

DOI: 10.1007/s11661-017-4066-1

© The Minerals, Metals & Materials Society and ASM International 2017

## I. INTRODUCTION

NICKEL-based superalloys are a special class of alloys that are known for excellent mechanical strength, resistance to thermal creep, and resistance to oxidation.<sup>[1–3]</sup> These alloys derive their special properties from the various alloying additions.<sup>[1,4]</sup> While Cr (1–20 pct by weight) imparts oxidation resistance to conventional Ni-based superalloys, Mo and W are added for solid solution strengthening and high temperature stability. The additions of Al and Ti form  $\gamma'$  precipitates which impart precipitation hardening, and B, Zr, and C strengthen the grain boundaries.<sup>[1,5,6]</sup> The oxidation resistance provided by Cr addition is exceedingly important in aggressive environments such as gas turbine engines.<sup>[5,7–15]</sup> In fact, in alloys such as IN 713 LC, wherein the matrix is depleted of Cr, the decreased oxidation resistance has to be compensated by higher Al content or thermal barrier coatings.<sup>[16–18]</sup> In the light of the importance of Cr in the oxidation resistance of Ni-based superalloys, a series of high Cr alloys have been developed, which contain 32–40 pct Cr. Some well-known alloys of this type are Inconel 617, 625, 671, and 690 along with Haynes G35 and VDM33. These alloys are prime candidates in aggressive environments in chemical and petrochemical industries, nuclear industry, and fertilizer manufacturing.

In the Ni-Cr phase diagram,<sup>[19,20]</sup> the Cr solubility in Ni is seen to decline sharply with decreasing temperature, leading to the precipitation of  $\alpha$ -Cr in the

two-phase region. Depending on the Cr content and the heat treatment cycles, different Cr-based precipitates with various morphologies such as cellular or discontinuous precipitation (DP) and continuous precipitation (CP)<sup>[1,19,21–30]</sup> can form in high Cr Ni-based superalloys. While  $M_{23}C_6$  type of carbides, in the form of DP, are known to form in Alloy 690 (30 pct Cr),<sup>[31]</sup>  $M_6C$  carbides and  $\delta$  phase are known to occur, respectively, in GH169 (18 pct Cr) and GH625 (22 pct Cr). While  $\alpha$ -Cr precipitation can occur in GH169 and GH625 after long-term aging, it is the major precipitate phase that can form in GH648 (33 pct Cr), GH837 (37 pct Cr), and GH840 (40 pct Cr) as DP lamellae or short-plates or star shapes depending on the heat treatment temperature and cycle.<sup>[32]</sup> The relative fractions of the different morphologies of precipitates can have serious implications on the mechanical properties, the ease of processing, and the corrosion resistance of the alloy.<sup>[12,32–36]</sup> The localized nature of DP can have relatively more adverse effects on the performance of the high Cr Ni-based alloys. Hence, it would be beneficial to determine the kinetics and mechanisms of DP and the temperature ranges of its dominance in isolation from the effects of other alloying elements. Therefore, the present study focuses on the kinetics, mechanisms, and the microstructural sensitivity of DP reaction in a high Cr (42 wt pct) Ni-based binary alloy system.

## II. EXPERIMENTAL

A cold rolled (70 pct reduction) piece of a binary alloy of Ni and Cr containing 42 pct Cr by weight was subjected to solutionizing at 1473 K (1200 °C), followed by water quenching, to attain a single-phase microstructure. This resulted in an average grain size of  $\sim 150 \mu\text{m}$ , as shown in Figure 1. Specimens in this  $\gamma$ -quenched state

N. KESKAR, A.K. PATTANAIK, K.V. MANI KRISHNA, D. SRIVASTAVA, and G.K. DEY are with the Mechanical Metallurgy Division, Materials Group, Bhabha Atomic Research Centre, Trombay, Mumbai, India 400085. Contact e-mail: nachiketkeskar@gmail.com, nachiket@barc.gov.in

Manuscript submitted October 5, 2016.

Article published online April 7, 2017

were subjected to aging heat treatments at various temperatures ranging from 923 K (650 °C) to 1123 K (850 °C) at intervals of 50 K (50 °C) for time periods of 1 to 6 hours.

The aged samples, electro-etched with 10 pct chromic acid at 6 V for 10 to 15 seconds, were characterized for microstructure in a Carl Zeiss Auriga CrossBeam<sup>®</sup> field emission gun scanning electron microscope. Electron backscattered diffraction and transmission Kikuchi diffraction (TKD) were carried out using an Oxford Nordlys Max2<sup>®</sup> system. For transmission electron microscopy (TEM) as well as TKD, the samples were prepared by the conventional technique, which involved initial slicing with a low-speed diamond saw, followed by mechanical grinding and polishing to a thickness of 100  $\mu\text{m}$ . Disks of 3 mm diameter punched out from these slices were then further thinned by electrojet thinning in a twin-jet electropolishing machine using perchloric acid and methanol in the ratio of 20:80 by volume at 243 K (−30 °C). For imaging using TKD, the sample was affixed in a specialized holder which ensured a clear line of sight between the electron beam transmitted through the sample and the TKD detector/camera. The critical SEM and TKD camera parameters employed for obtaining the TKD image included a working distance of 3 mm, an aperture size of 120  $\mu\text{m}$ , an accelerating voltage of 30 kV along with a TKD scan step size of 15 nm at a TKD camera binning of  $2 \times 2$  to give a TKD pattern acquisition rate of 60 Hz. Quantitative compositional characterization using energy-dispersive spectroscopy (EDS) and high-angle annular dark field (HAADF) imaging was carried out in a Carl Zeiss Libra 200FE<sup>®</sup> TEM.

### III. RESULTS

The results section is divided into four sub-sections detailing the microstructure evolution, the characterization of the precipitate phase, the kinetics of

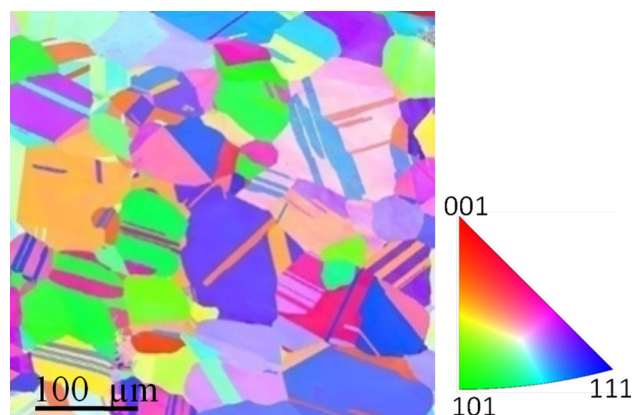


Fig. 1—The inverse pole figure color coded map of the starting microstructure obtained by solutionizing and water quenching from 1473 K (1200 °C).

precipitation, and the location selectivity of precipitation, respectively.

#### A. Microstructure Evolution

The single-phase  $\gamma$ -quenched microstructure (see Figure 1 inset) was seen to decompose into a two-phase microstructure as a result of the different heat treatments that were applied to the samples. ‘Cells’ of colonies of parallel precipitate lamellae were formed as a result of matrix decomposition *via* discontinuous precipitation (DP) mechanism.<sup>[37]</sup> The DP was characterized by certain typical features, which have been representatively shown in the SEM and TEM images in Figure 2. The DP cells in the present alloy originated from the grain boundaries, as shown in Figure 2(a). Figure 2(b) shows the region near the initiation site of a DP cell containing some partly grown grain boundary precipitates as well as some parallel precipitate lamellae. In order to form a DP cell, the grain boundary precipitates grew in a direction away from the initiating grain boundary and formed an advancing ‘front’; a reaction front (RF)<sup>[21–24,38–40]</sup> which delineated the boundary between the transformed and the untransformed region, as shown in the Figure 2(c). The growth of a DP cell took place not only by growth of the lamellae but also by the branching of the existing lamellae.<sup>[41]</sup> As shown in Figure 2(d), in cases where the growth of a colony is restricted, the lamellae in the colony with restrained growth showed coarsening, while the growth of the DP cell as a whole continued. Due to coarsening of older and/or restrained colonies, the interlamellar spacing ( $\lambda$ ) was seen to be relatively finer near the RF (newer colonies) and coarser near the original grain boundary (older colonies). Figures 2(e) and 2(f) show the initial stages of the growth of a DP cell. In these figures, the predisposition of the grain boundary precipitates toward certain directions/orientations was observed. The direction of the growth of the initial grain boundary precipitates was seen to dictate the direction of the migration of the grain boundary, and thereby that of the DP cell. The originating grain boundary and the RF can also be seen in the HAADF image of a DP cell shown in Figure 2(g). Figure 3 shows occasions of DP cells growing into opposite grains from adjacent sections of a shared grain boundary. Such instances of ‘S’ and double-seam morphology<sup>[42,43]</sup> could be observed at all the aging temperatures explored in this study.

Aging the single-phase samples at different temperatures for the same time period (2 hour) resulted in noticeable changes in the microstructures as seen in Figure 4. While the DP cells formed at 923 K (650 °C) were close to the initiation stages (see Figure 4(a)), those formed at 973 K (700 °C) were larger and showed easily discernable parallel lamellae, as seen in Figure 4(b). Also, at 973 K (700 °C), some continuous precipitation (CP) could be noted (see Figure 4(b)). Aging at a temperature of 1023 K (750 °C) resulted in an increase in the extent of DP as well as CP, as seen in Figure 4(c). On increasing the aging temperature to 1073 K (800 °C) (see Figure 4(d)), noticeably large area fractions of

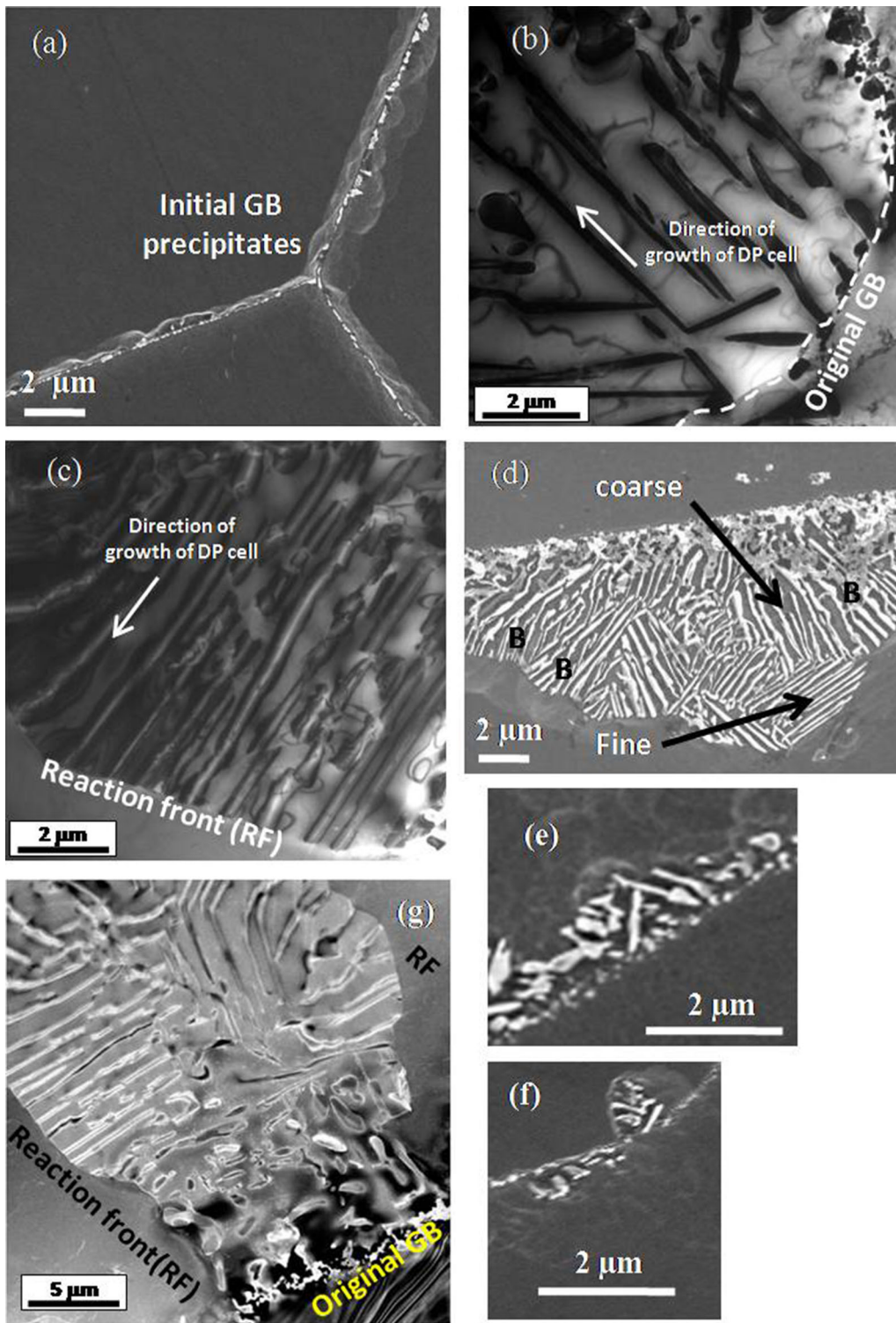


Fig. 2—Microstructures of sample aged at 1023 K (750 °C) for 2 h showing, (a)  $\gamma$ -Ni boundaries showing initial grain boundary (GB) precipitates, (b) a DP cell and its originating GB, (c) the reaction front of a DP cell, (d) DP cell showing branching (marked as 'B') and coarsening of the lamellae. (e) and (f) show the near-GB precipitates conforming to particular orientations in a sample aged at 973 K (700 °C) for 1 h. (g) HAADF image of a DP cell (1023 K or 750 °C for 2 h). (a), (d), (e), and (f) are SEM images, while (b), (c), and (g) are TEM images.

grains were seen to have undergone DP, while CP appeared to be suppressed. In fact, at several locations, separate DP cells merged together and covered an entire

grain. The microstructure evolved after aging at 1123 K (850 °C) showed more instances of CP as compared to DP, as shown in Figure 4(e). At this temperature,



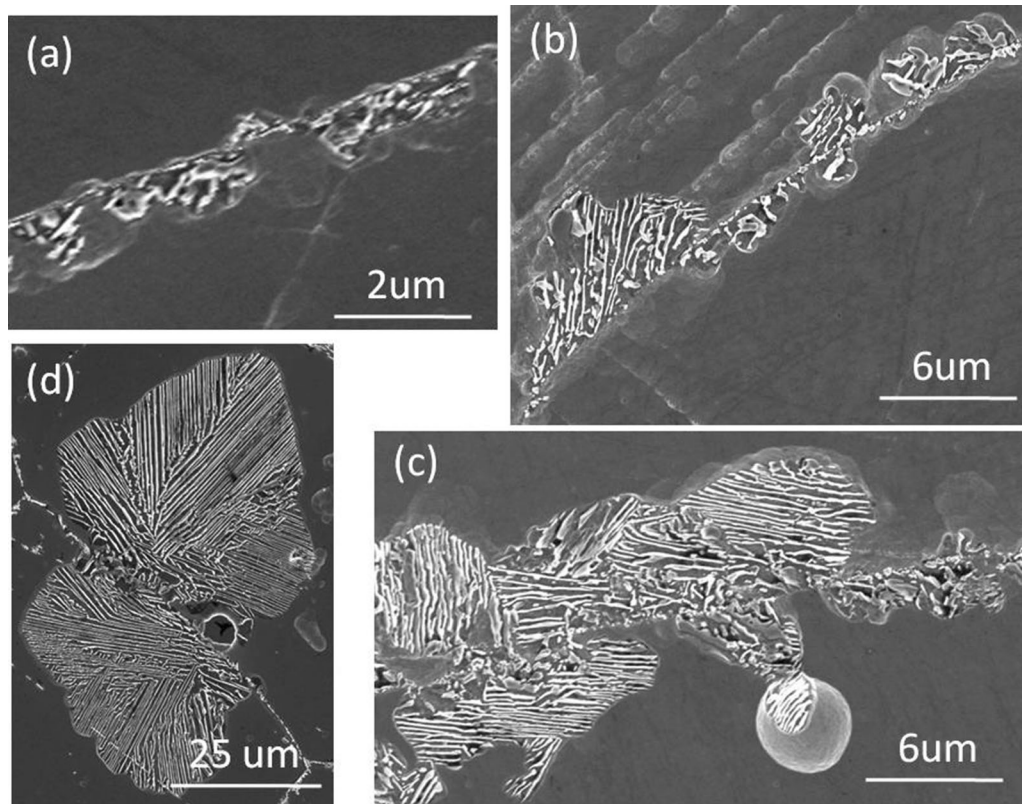


Fig. 3—Microstructures of sample aged at (a) 923 K (650 °C), (b) 973 K (700 °C), (c) 1023 K (750 °C), and (d) 1123 K (850 °C) for 2 h each, showing instances of ‘S’ and double-seam morphology of DP cells.

instances of arrest of DP cell growth due to CP could also be seen. Finally, at 1173 K (900 °C), as shown in Figure 4(f), all precipitation was seen to occur in CP morphology.

### B. Characterization of Precipitate Phase

The compositional difference between the precipitate and the matrix indicated by the HAADF image shown in Figure 2(e) was further explored by TEM-based EDS analysis in a sample aged at 1023 K (750 °C) for 2 hour (see Figure 5). This showed Cr enrichment of the precipitate lamellae and the corresponding Cr depletion in the interlamellar region within the DP cell. The lamella was found to have, on an average, 82 pct by weight Cr and correspondingly 18 pct by weight Ni. In the region within the DP cell just adjacent to the lamella, the Cr content dropped to 39 pct, while Ni content rose to 61 pct. The Ni content in the interlamellar region reached a maximum value of 73 pct. This systematic and complementary variation in the Cr and Ni content across the precipitate lamellae was brought out clearly by an EDS line scan (see inset in Figure 5). In contrast to this gradual compositional variation within the DP cell, a sharp and discontinuous compositional change of the matrix  $\gamma$  phase across the RF (73 pct in the interlamellar region as opposed to 58 pct in the undecomposed matrix region) could be seen.

In order to confirm the identity of the precipitate phase, X-ray diffraction patterns, taken from samples

aged at 1073 K (800 °C) for different time periods (1, 3, and 6 hour), were analyzed. These diffraction spectra showed a progressive increase in the intensity of the peak from  $\alpha$ -Cr phase, as seen in Figure 6(a). Additionally, the adjoining microstructures showed progressive increase in the volume fraction of the precipitates with increasing aging times. Thus, these observations established the evolution of the  $\alpha$ -Cr phase.

On closer examination of the  $\gamma$ -Ni peaks, it could be seen in Figure 6(b) that the peaks for  $(111)_{\text{Ni}}$ ,  $(200)_{\text{Ni}}$ , and  $(220)_{\text{Ni}}$  showed a shift toward higher  $2\theta$  values as the aging time was increased from 1 to 6 hour. Higher  $2\theta$  values, being indicative of smaller  $d$ -spacing, the average  $d$ -spacing reduced with increasing aging time. Thus, this observation confirmed the shrinking of the Ni-Cr lattice due to the diffusion of the larger Cr atoms out of the solid solution.<sup>[44]</sup>

The orientation relationship between the lamellar precipitate and the matrix phases, indicated by the morphology of the grain boundary precipitates in Figure 2(e) and (f), was determined using orientation maps generated by TKD method<sup>[45–47]</sup> as well as from TEM-based selected area diffraction (SAD) patterns. Figure 7(a) shows the inverse pole figure and phase maps of a selected region of a DP cell which had grown in a sample aged at 1023 K (750 °C) for 6 hour. The misorientation between the interlamellar matrix and the precipitate phases was found to be  $42^\circ @ [-5 -5 -28]$ . This compared well with the Kurdjumov-Sachs orientation relationship ( $42.8 \text{ deg} @ [2 2 11]$  or  $\{111\}_\gamma$

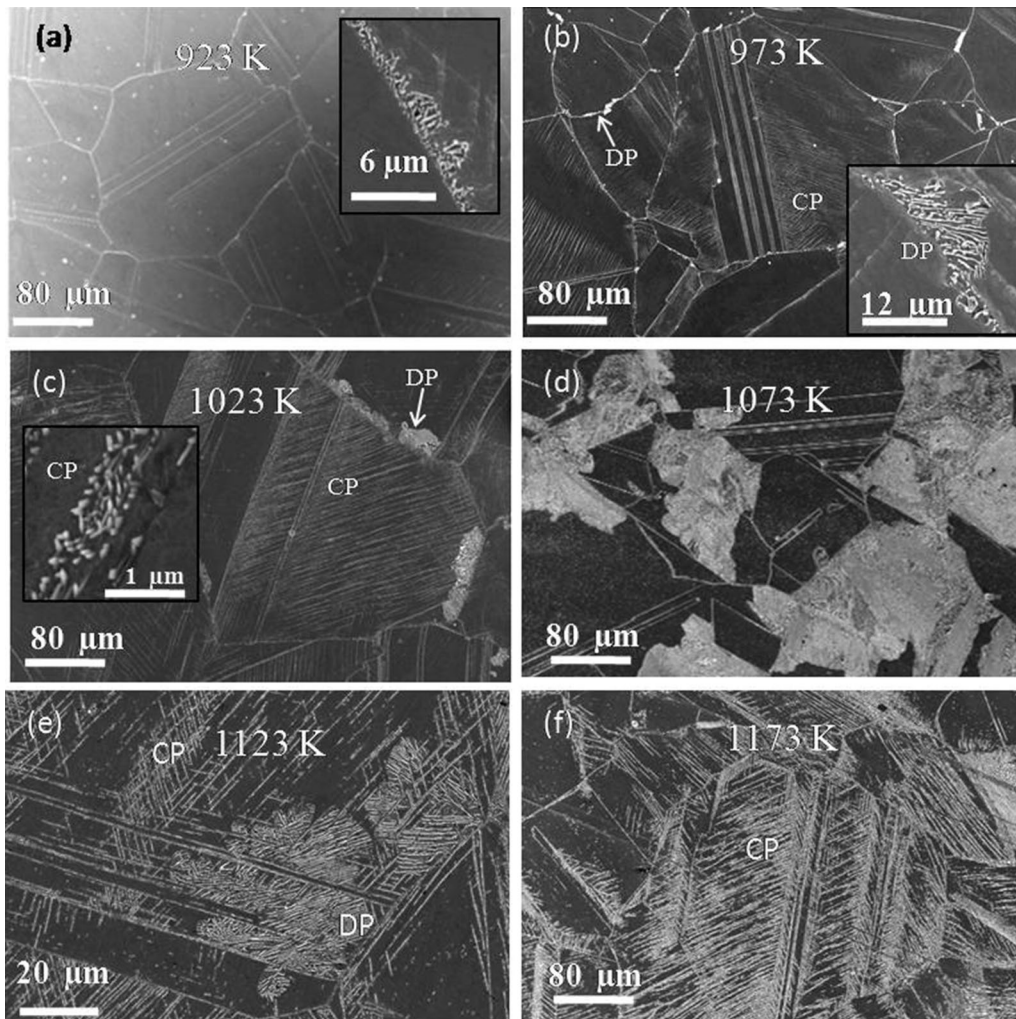


Fig. 4—SE micrographs showing the microstructure that evolved upon aging at (a) 923 K (650 °C), (b) 973 K (700 °C), (c) 1023 K (750 °C), (d) 1073 K (800 °C), (e) 1123 K (850 °C), and (f) 1173 K (900 °C) for 2 h each. CP and DP stand for continuous and discontinuous precipitation, respectively.

$\{110\}_\alpha$  and  $\langle 1-10 \rangle_\gamma \parallel \langle 1-11 \rangle_\alpha$  known to exist between a bcc phase precipitating out of an fcc matrix.<sup>[26]</sup> Figure 7(b) shows the superimposed SAD patterns from [111] zone axis of bcc Cr and [110] zone axis of fcc Ni, conforming to the Kurdjumov-Sachs orientation relationship.

### C. Precipitation Kinetics

The parameters of  $\lambda$  and RF velocity ‘ $v$ ,’ which are the characteristics of the kinetics of DP cell growth, were determined from the quantitative analysis of the experimentally observed microstructures. The average  $\lambda$  increased with the aging temperature, see Figure 8(a). Correspondingly, the inverse of the interlamellar spacing ( $1/\lambda$ ) was seen to approach 0 (*i.e.*, infinite  $\lambda$ ) at  $\sim 1138$  K (865 °C). The infinite  $\lambda$  value represents the termination of DP cell formation<sup>[28]</sup> and hence, this is the maximum temperature upto which DP is expected to occur in this alloy.

The velocity of the RF,  $v$ , was derived from the experimentally measured values of the average width ( $w$ ) of the DP cells. The value of ‘ $w$ ’ was seen to be a function of temperature as well as time (see Figures 8(b) and (c)). The increase in the aging temperature (for a fixed time duration of 2 hour) was seen to result in an increase in the average width ( $w$ ) of the DP cells, as shown in Figure 8(b). The value of ‘ $w$ ’ reached a maximum of  $\sim 60$   $\mu\text{m}$  (in 2 hour) at the temperature of  $\sim 1073$  K (800 °C). Additionally, Figure 8(c) depicts dependence of the ‘ $w$ ’ vs time curves on the aging temperature. While the average slope of the ‘ $w$ ’ vs time curve (*i.e.*, ‘ $v$ ’) at 1073 K (800 °C) was higher than that at 1023 K (750 °C), the slope at 1123 K (850 °C) was of an intermediate value. Thus, the value of ‘ $v$ ’ also reached a maximum of  $\sim 10^{-8}$  m/s at the temperature of  $\sim 1073$  K (800 °C), as demonstrated in Figure 8(d). It may be noted that to account for the variation induced by the difference between the plane of observation and the cell growth directions, the average interlamellar spacing,  $\lambda$ , was normalized as



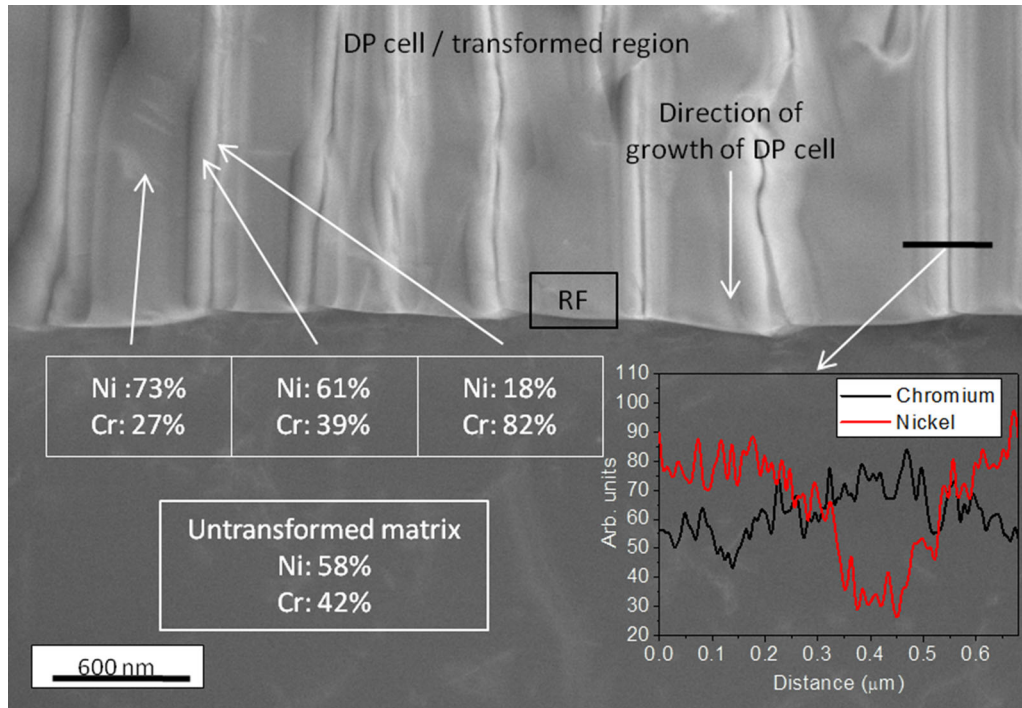


Fig. 5—TEM-based EDS analysis of the elemental composition at different locations in a DP cell. The inset shows the composition variation across a precipitate lamella along the black line.

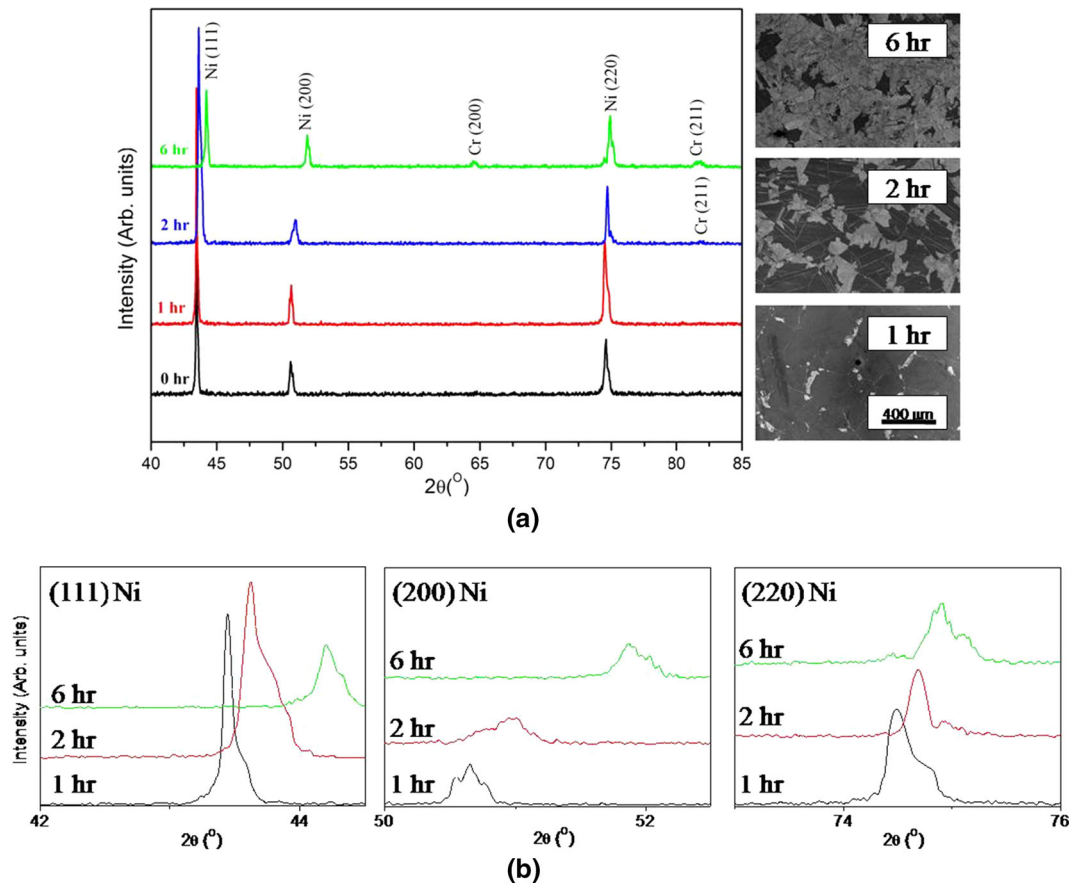


Fig. 6—(a) XRD spectrum profiles for samples aged at 1073 K (800 °C) for different time periods and the corresponding microstructures. (b) Shift in Ni phase peaks observed as a result of different aging time periods.

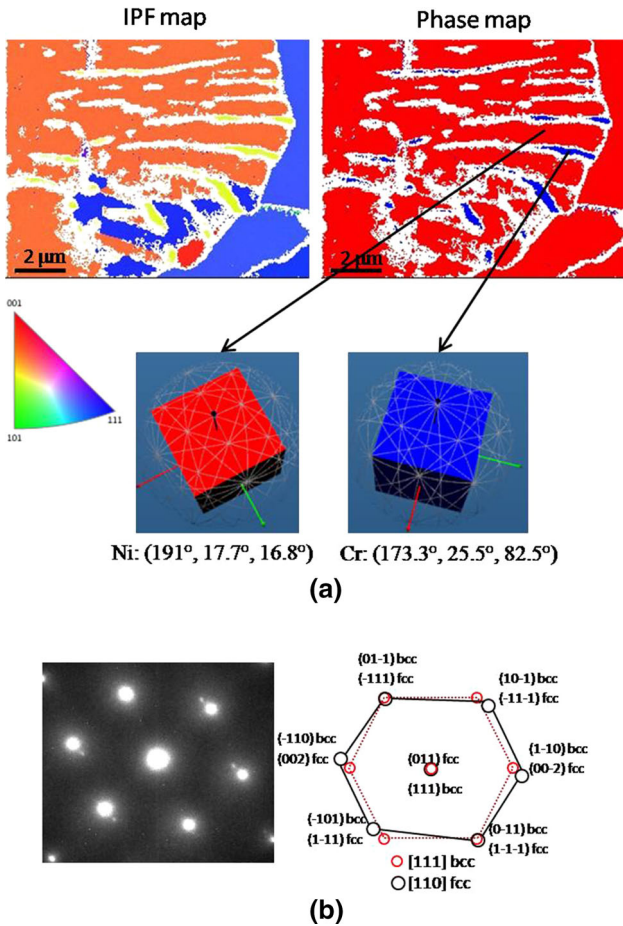


Fig. 7—(a) Transmission Kikuchi diffraction (TKD) images of a DP cell; sample aged at 1023 K (750 °C) for 6 h. Local orientations of Ni and Cr lattices are also shown in Euler angle notations, along with graphic representation of the orientation of the respective unit cells. (b) Superimposed SAD patterns from precipitate and matrix conforming to the Kurdjumov–Sachs orientation relationship.

$$\lambda = \frac{\pi}{4} \times \lambda_{\text{average}} \quad [1]$$

Similar normalization was also carried out for the DP cell width,  $w$ .<sup>[21,48]</sup>

Three kinetic models, *viz.*, Turnbull,<sup>[46,48,49]</sup> Aaronson–Liu,<sup>[49]</sup> and Petermann–Hornbogen,<sup>[50]</sup> were used in this study to understand the kinetics of the DP reaction in terms of the grain boundary diffusivity triple product of Cr diffusing in  $\gamma$ -Ni. The grain boundary diffusivity triple product ( $P$ ) is given by  $s\delta D_b$ , where  $s$  is the segregation factor,  $\delta$  is the grain boundary thickness, and  $D_b$  is the grain boundary diffusion coefficient. The expressions for  $P$  from each of the three models are given in Table I, and the parameters required for these expressions are enlisted in Table II. While the parameters of  $\lambda$  and ‘ $v$ ’ were measured directly from the microstructures, the solute concentrations ( $x_0$ ,  $x_1$  and  $x_2$ ) were calculated from the equilibrium Ni–Cr phase diagram and  $\Delta G_C$  was calculated from the free energy vs composition diagram generated using Thermo-Calc<sup>®</sup><sup>[49]</sup> software.

The values of  $P$ , obtained from the aforementioned three kinetic models at different temperatures, have been plotted in Figure 9(a). A comparison of these with the  $P$  values obtained from radiotracer experiments ( $P_R$ )<sup>[51,52]</sup> showed that a single model was insufficient to describe the kinetics at all the temperatures investigated in this study. At lower temperatures, the  $P$  estimated using the Turnbull model was found to be in good agreement with that of the  $P_R$  (with deviation of 3 pct). On the other hand, in the higher temperature regime, even the closest model (Aaronson–Liu) in terms of deviation from  $P_R$  value had a deviation of 93 pct, see Figure 9(b).

The temperature dependence of  $P$  is shown in Figure 10.  $P$  was seen to be a function of temperature in the form of an Arrhenius equation,

$$P = P_0 e^{-\frac{Q_b}{RT}}, \quad [2]$$

where  $P_0$  is the pre-exponential factor and  $Q_b$  is the activation energy. These two Arrhenius parameters were calculated from Figure 10 and presented in Table III. While the Turnbull model yielded  $Q_b = 307.5$  kJ/mol and  $P_0 = -4.95$ , the Aaronson–Liu model resulted in  $Q_b = 278.5$  kJ/mol and  $P_0 = -7.83$ , and the Petermann–Hornbogen model resulted in  $Q_b = 374.2$  kJ/mol and  $P_0 = -1.50$ . Comparing these values with those reported in literature<sup>[51]</sup> for grain boundary diffusion of <sup>51</sup>Cr in Ni–30Cr alloy, the Aaronson–Liu model appears to be the overall best fit for this alloy composition over the studied range of temperatures.

#### D. Grain Boundary Selectivity in DP

It was observed that not all grain boundaries showed the formation of DP cells. For example, in the specimen aged at 1023 K (750 °C) for 6 hour (see Figure 11(a)), some grain boundaries were seen to be devoid of any DP cells, while some others showed a copious growth of such cells. Even among the grain boundaries which did show the growth of DP cells, the cell width was different in each instance. This was an indication of the variations in rate of nucleation and growth of DP cells as a function of the misorientation angle of the grain boundaries (*i.e.*, nature of boundaries). In order to investigate these variations, the distribution of misorientation angles was plotted for (a) all grain boundaries of the representative microstructure (b) boundaries containing DP cells. As can be seen in Figure 11(b), the microstructure had a dominant presence of 60 deg  $\langle 111 \rangle$  type of twin boundaries (CSL type of boundaries with  $\Sigma = 3$ ) which corresponded to the peak at 60 deg in the misorientation angle distribution. On the other hand, the misorientation distribution profile of those grain boundaries, which showed nucleation of DP cells, had a peak at  $\sim 45$  deg misorientation.

To further explore the implications of the nature of the grain boundary on the nucleation and growth of DP cells, the grain boundaries at which DP cells had nucleated were partitioned into near-CSL and ordinary grain boundaries, based on their misorientation. The deviations from the ideal CSL misorientations were calculated for those boundaries which were classified

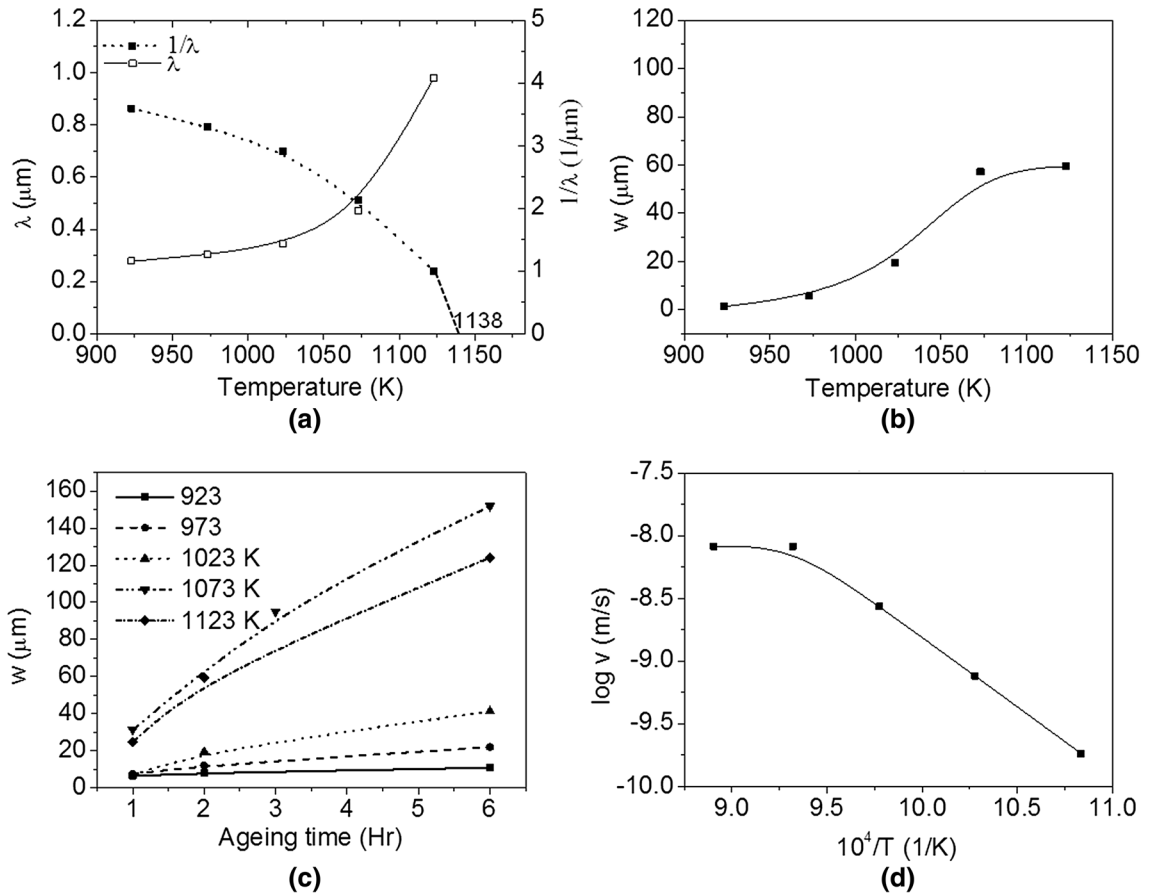


Fig. 8—(a) Variation of  $\lambda$  and its inverse,  $1/\lambda$ , with the aging temperature. (b) Variation of  $w$ , with the aging temperature for a fixed time duration (2 h). (c) Variation of  $w$ , as a function of aging time at different aging temperatures. (d) Variation of  $v$  with the aging temperature.

Table I. Expressions for Grain Boundary Diffusivity Triple Product (P) Using Three Kinetic Models

Model	Expression	Variables
Turnbull	$P = \frac{x_0}{x_0 - x} v \lambda^2$	$x_0$ = the initial solute content in the supersaturated $\gamma$ phase $x_1$ = the equilibrium solute content in the $\gamma_0$ phase
Aaronson–Liu	$P = \frac{x_2 - x_0}{4(x_2 - x_1)} v \lambda^2$	$x_2$ = the equilibrium solute content in the $\alpha$ phase at a particular temperature $v$ = the RF velocity $\lambda$ = the average interlamellar spacing at a particular temperature
Petermann–Hornbogen	$P = \frac{RT}{8\Delta G} v \lambda^2$ $\Delta G = \Delta G_c + \Delta G_\gamma$ $\Delta G_\gamma = 2\gamma V_m / \lambda$	$R$ = the universal gas constant $\Delta G$ = the driving force for DP in terms of the overall change in the Gibbs energy $\Delta G_c$ = Chemical free energy $\Delta G_\gamma$ = Interfacial free energy $V_m$ = the molar volume of the $\gamma$ -Ni phase = $6.58 \times 10^{-6} \text{ m}^3/\text{mol}$ $\gamma$ = the interfacial energy for the $\gamma$ -Ni/ $\alpha$ -Cr interface = $200 \text{ mJ/m}^2$ at 0 K ( $-273 \text{ }^\circ\text{C}$ ) <sup>[50]</sup> The interfacial energy for the other temperatures was calculated according to $d\gamma/dT = 0.1 \text{ mJ/m}^2\text{K}$

near-CSL boundaries, and the corresponding cell widths 'w' were plotted against such deviations. It is evident from Figure 12 that the extent of cell growth was increasing with that of the deviation of that boundary from ideal CSL misorientations.

#### IV. DISCUSSION

Three important aspects of this study deserve to be discussed in further details. Firstly, the DP cell growth occurring in the present alloy system is seen to follow



**Table II. Input Variables for the Kinetic Models**

T (°C) (K)	$\lambda$ ( $\mu\text{m}$ )	$v$ ( $\text{\AA}/\text{s}$ )	$x_1$	$x_2$	$-\Delta G_c$ (J/mol)	$\gamma$ (mJ/m <sup>2</sup> )	$\Delta G_\gamma$ (J/mol)
923 (650)	0.28	1.84	0.31	0.99	440	292.3	13.8
973 (700)	0.30	7.64	0.32	0.985	330	297.3	12.9
1023 (750)	0.34	27.20	0.34	0.98	220	302.3	11.6
1073 (800)	0.47	82.46	0.35	0.975	110	307.3	8.6
1123 (850)	0.99	152.0	0.37	0.97	50	312.3	4.1

**Table III. Arrhenius Parameters Obtained from the Three Kinetic Models Along with Those Obtained by Radiotracer Experiments**

Parameters	Turnbull	Aaronson-Liu	Petermann-Hornbogen	Grain boundary diffusion of <sup>51</sup> Cr in Ni-30Cr <sup>[51,52]</sup>
$\log P_0$ (m <sup>3</sup> /s)	-4.95	-7.83	-1.50	-8.54
$Q_b$ (kJ/mol)	307.5	278.5	374.2	245.5

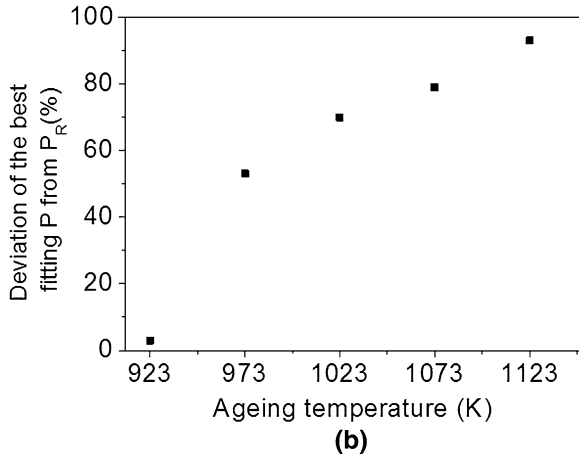
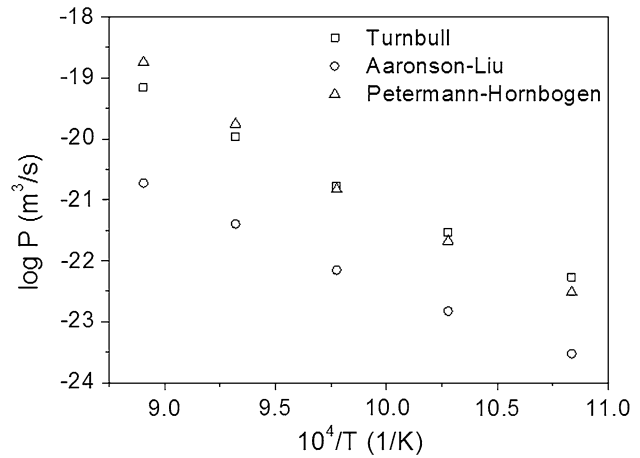
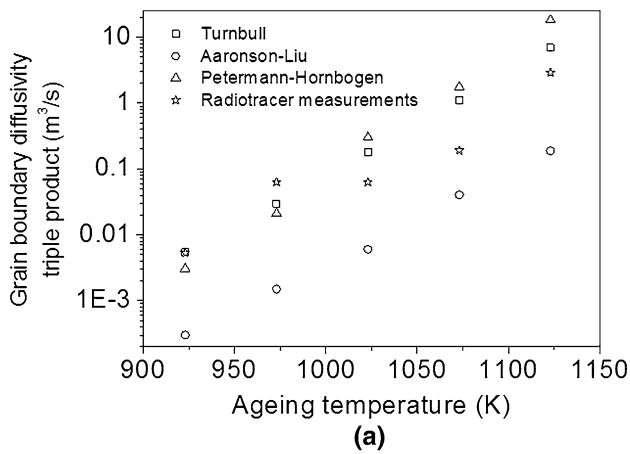


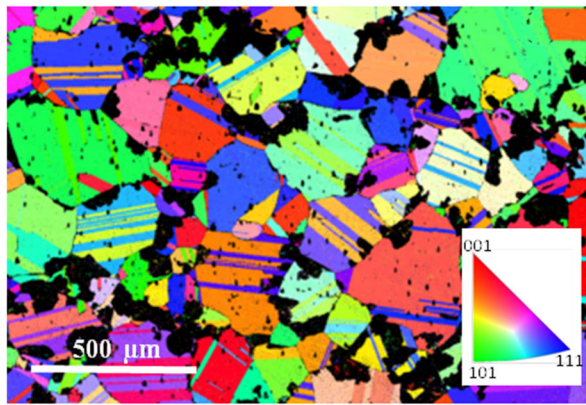
Fig. 9—(a) Values of the  $P$  obtained from the three models along with  $P_R$ , at different temperatures. (b) Deviation of the closest fitting  $P$  from the  $P_R$  at different temperatures.

Fig. 10—Arrhenius plots of  $P$ , obtained from kinetic models of Turnbull, Aaronson-Liu, and Petermann-Hornbogen.

of the growth of DP was strongly governed by the nature of the originating grain boundary. These aspects are discussed in greater detail below.

#### A. Mechanism of Growth of DP Cells

Cellular or discontinuous precipitation (DP) is a mode of relaxation of a thermodynamically metastable state of a supersaturated alloy by the redistribution of solute *via* nucleation and growth of second phase precipitates.<sup>[8,21,24,28,40,53,54]</sup> Of the multiple theories used to explain DP,<sup>[27,41,43,54,55]</sup> the ‘precipitate driven grain boundary migration,’ also known as the ‘pucker’ mechanism, as suggested by Tu and Turnbull,<sup>[41,54,55]</sup> appeared to be at play in this alloy. Figures 2(e) and (f) showed that the initial precipitation occurred with a particular orientation relationship to the  $\gamma$  matrix on the trailing/decomposed side of the RF. This orientation relationship was quantitatively confirmed to be of the Kurdjumov-Sachs type from the TKD mapping as well as from TEM-based SAD patterns, as



(a)

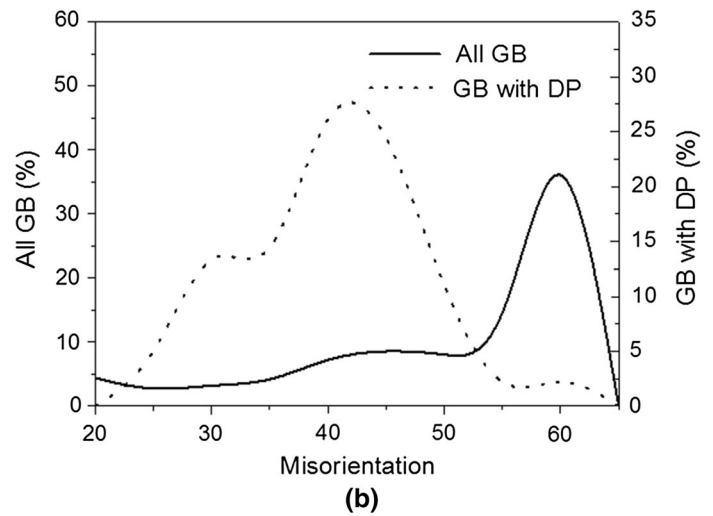


Fig. 11—(a) Specimen aged at 1023 K (750 °C) for 6 h showing DP cells (black patches) growing from various grain boundaries. (b) Overall distribution of grain boundaries over a sampling area overlaid with the distribution of grain boundaries that show DP cell nucleation.

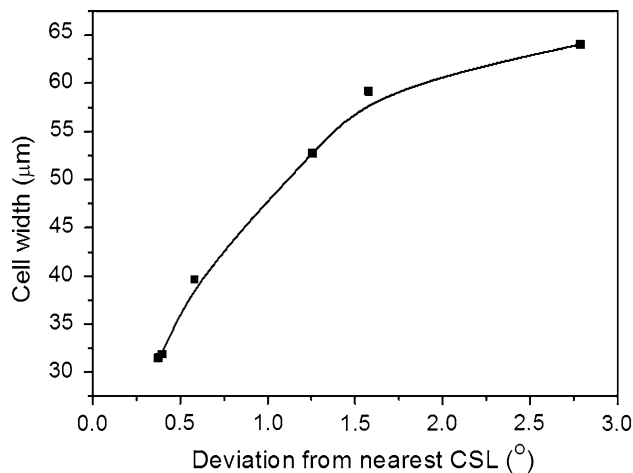


Fig. 12—Variation of the DP cell width,  $w$ , with the deviation of the nucleating boundary from the ideal CSL angle.

shown in Figure 7. Such precipitates have a coherent interface on one side and a semi- or incoherent interface on the other.<sup>[41,43]</sup> The grain boundary, in order to minimize the incoherent interface, migrates along the incoherent interface up to the tip of the precipitate, thus embedding the precipitate in the matrix. Repetitions of this mechanism of grain boundary migration along the incoherent interface of the precipitate lead to the formation of the lamellar structure. Thus, the RF or the grain boundary migrates in the direction of growth of the precipitates.

### B. Kinetics of DP Cell Growth

While the three kinetic models (Tu–Turnbull, Aaronson–Liu, and Petermann–Hornbogen) employed in the present study are well established, these are limited by their inherent assumptions. Consequently, from Figure 9(a), it can be clearly seen that no model was suitable for all the investigated temperatures; the

suitability being adjudged by the comparison of the  $P$  value to the  $P_R$  value at that particular temperature. The value of  $P_R$ , being a direct measurement of diffusivity, can be considered as the reference value for the validation of the ‘indirect’ kinetic models. The graph shown in Figure 9(b) demonstrates that, while at lower temperatures, the  $P$  value from the closest fitting model (at that temperature) was found to differ from  $P_R$  by only 3 pct, at higher temperatures, the difference between the two ( $P$  and  $P_R$ ) was as high as 93 pct. This difference was seen to increase progressively with the aging temperature, thus pointing toward the increasing limitations of the models at elevated temperatures. A possible explanation for this is the increasing dominance of CP at higher temperatures.

The diffusivity of substitutional solute atoms is known to be much faster along grain boundaries as compared to that in the bulk lattice, especially at relatively lower temperatures.<sup>[56]</sup> At elevated temperatures, however, the advantage of fast diffusion along the grain boundaries is reduced, since bulk diffusivity is also enhanced. At relatively higher temperatures, thus, continuous precipitation (CP) is expected to come into the picture, since the higher temperatures can initiate and sustain the bulk diffusion required for continuous nucleation and growth.<sup>[22,25,30,39,40]</sup> When CP occurs, the degree of supersaturation in the matrix phase, which provides the driving force for DP, is lowered and this enables CP to compete with DP. Furthermore, the presence of continuous precipitates may pose a physical restriction to RF migration. Thus, as seen in Figure 4(e), the growth of a DP cell can be hindered, chemically and/or physically, due to the CP. As was evident from Figures 8(c) and (d), the velocity of RF migration was seen to reduce at temperatures higher than 1073 K (800 °C). This demonstrates the retarding effect of CP on the kinetics of DP at elevated temperatures. In fact, as observed from Figure 8(a), the DP tends to stop at ~1138 K (865 °C) as a result of loss of the driving force of supersaturation on account of extensive CP and no

DP was observed at 1173 K (900 °C). Thus, while the kinetic models, which are mathematical representations of precipitation in the discontinuous mode, were fairly accurate at relatively lower temperatures (at which DP is dominant), the accuracy of these models was diminished at elevated temperatures at which CP also came into the picture.

The kinetics of the DP cell growth could be best explained by the Turnbull model at lower temperatures [923 K and 973 K or (650 °C and 700 °C)] and by the Aaronson–Liu model at higher temperatures [1123 K and 1173 K or (850 °C and 900 °C)]. At lower temperatures, the diffusivity is lesser and correspondingly, the growth of DP cell is also slower, as seen in Figure 8(d). Consequently, the strong initial concentration gradient between the initial and equilibrium matrix phase remains nearly unchanged for a considerable duration of time and this continues to provide the driving force for DP cell growth. Hence, at lower aging temperatures, the Turnbull model, which is essentially based only on the concentration gradient between the initial and equilibrium matrix phase, is the best fit.

At higher temperatures, the enhanced rate of DP cell growth brings the overall matrix decomposition process closer to the steady state condition. On one hand, the Turnbull theory considers the difference between the prevalent and equilibrium composition of the matrix phase to be constant for the duration of the DP reaction. On the other hand, the Aaronson–Liu model takes into account the solute depletion from the matrix during the decomposition. Thus, the Aaronson–Liu model incorporates the change in the prevalent composition of the matrix phase, which is a more realistic depiction of the DP at higher temperatures. Hence, this model had the least deviation (93 pct) among other models at higher temperatures, at which the DP process was closer to equilibrium state as compared to the DP process at lower temperatures.

### C. Effect of the Nature of the Originating Grain Boundary

The significant grain boundary selectivity for the formation of DP cells as brought out in this study can be rationalized by the differences in the energies of the participating grain boundaries. It is known that the mechanism of the DP reaction is the solute diffusion along grain boundaries. Hence, it is reasonable to expect that grain boundaries with different energies would promote the DP reaction to different extents. This was evident in Figure 11(b), which showed very little DP cell formation on  $\Sigma 3$  boundaries and profuse DP cell formation on high-energy ordinary high-angle boundaries, although the  $\Sigma 3$  boundaries were more numerous in the microstructure. The 60 deg  $\langle 111 \rangle$  type of twin boundaries ( $\Sigma 3$  boundaries), though high angle, are low-energy boundaries. Hence, the propensity for DP cell nucleation and growth is lesser for these twin boundaries, in spite of being statistically more probable. Additionally, in case of  $\Sigma 3$  boundaries, the grain boundary energy is known to increase with an increase in the deviation from the ideal CSL condition.<sup>[57]</sup> Hence,

the  $\Sigma 3$  boundaries with larger deviation from ideal CSL configuration showed a farther extent of DP cell growth. Thus, Figure 12 implies that the extent of cell growth increased with increasing grain boundary energy. In summary, high-energy grain boundaries were seen to promote DP cell nucleation and growth.

## V. CONCLUSIONS

The Ni-42 wt pct Cr alloy was seen to undergo discontinuous precipitation *via* the “precipitate driven grain boundary migration” mechanism suggested by Tu and Turnbull at all temperatures in the range of 923 K to 1123 K (650 °C to 850 °C), albeit to different extents.

1. CP and DP were seen to be competing modes of decomposition in the present alloy system. While DP was dominant at lower temperatures, significant contribution from CP was observed at higher temperatures. The maximum temperature upto which DP cell nucleation occurs was estimated to be ~1138 K (865 °C).
2. It was found that upto a temperature of 973 K (700 °C), the Turnbull model was a more accurate description of DP kinetics, while at higher temperatures (upto 1123 K, 850 °C), the Aaronson–Liu model was a better representation.
3. The DP reaction was seen to prefer high-energy grain boundaries over low-energy boundaries, such as  $\Sigma 3$  boundaries. The DP cells nucleating at low-energy CSL boundaries also appeared to prefer the CSL boundaries with larger deviation from ideal CSL configuration, that is, those with higher energies.

## REFERENCES

1. R.C. Reed: *The Superalloys: Fundamentals and Applications*, Cambridge University Press, New York, 2006.
2. T. Pollock and S. Tin: *J. Propuls. Power*, 2006, vol. 22, pp. 361–74.
3. M. Durand-Charre: *The Microstructure of Superalloys*, Gordon and Breach Science Publishers, Canada, 1997.
4. A.K. Jena and M.C. Chaturvedi: *J. Mater. Sci.*, 1984, vol. 19, pp. 3121–39.
5. R.A. MacKay, T.P. Gabb, A. Garg, R.B. Rogers, and M.V. Nathal: *Mater. Charact.*, 2012, vol. 70, pp. 83–100.
6. N. D’Souza, M. Newell, K. Devendra, P.A. Jennings, M.G. Ardakani, and B.A. Shollock: *Mater. Sci. Eng. A*, 2005, vols. 413–414, pp. 567–70.
7. P. Brož, J. Buršík, M. Svoboda, and A. Kroupa: *Mater. Sci. Eng. A*, 2002, vol. 324, pp. 28–33.
8. Y.Q. Chen, T.J.A. Slater, E.A. Lewis, E.M. Francis, M.G. Burke, M. Preuss, and S.J. Haigh: *Ultramicroscopy*, 2014, vol. 144, pp. 1–8.
9. F. Pyczak, B. Devrient, F.C. Neuner, and H. Mughrabi: *Acta Mater.*, 2005, vol. 53, pp. 3879–91.
10. G.B. Viswanathan, R. Shi, A. Genc, V.A. Vorontsov, L. Kovarik, C.M.F. Rae, and M.J. Mills: *Scr. Mater.*, 2015, vol. 94, pp. 5–8.
11. Z. Bi, J. Dong, L. Zheng, and X. Xie: *J. Mater. Sci. Technol.*, 2013, vol. 29, pp. 187–92.
12. L. Zheng, C. Xiao, G. Zhang, B. Han, and D. Tang: *J. Alloys Compd.*, 2012, vol. 527, pp. 176–83.
13. A.S. Suzuki, K. Kawagishi, T. Yokokawa, and H. Harada: *Surf. Coat. Technol.*, 2012, vol. 206, pp. 2769–73.
14. M.I. Solonin: *Met. Sci Heat Treat.*, 2005, vol. 47, pp. 328–332.



15. X.-P. Tan, J.-L. Liu, T. Jin, X.-F. Sun, and Hu. Z.-Q.: *Trans. Nonferrous Met. Soc. China*, 2011, vol. 21, pp. 1004–1008.
16. L. Kunz, P. Lukáš, and R. Konečná: *Eng. Frac. Mech.*, 2010, vol. 77, pp. 2008–15.
17. L. Kunz, P. Lukáš, R. Konečná, and S. Fintová: *Int. J. Fatigue*, 2012, vol. 41, pp. 47–51.
18. M. Kianicová, J. Kafřík, and J. Trník: *Proc. Eng.*, 2016, vol. 136, pp. 346–52.
19. P. Nash: *Bull. Alloy Phase Diagr.*, 1986, vol. 7, pp. 466–76.
20. [www.calphad.com](http://www.calphad.com): 2006.
21. I. Manna, S.K. Pabi, and W. Gust: *Acta Metall. Mater.*, 1991, vol. 39, pp. 1489–96.
22. I. Manna, W. Gust, and B. Predel: *Scr. Metall. Mater.*, 1990, vol. 24, pp. 1635–40.
23. I. Manna, S.K. Pabi, and W. Gust: *Int. Mater. Rev.*, 2001, vol. 46, pp. 53–91.
24. I. Manna, J.N. Jha, and S.K. Pabi: *Scr. Metall. Mater.*, 1993, vol. 29, pp. 817–22.
25. I. Manna, P.K. Bala, S.K. Pabi, and W. Gust: *Acta Mater.*, 1996, vol. 44, pp. 4587–95.
26. C.P. Luo and G.C. Weatherly: *Acta Metall.*, 1987, vol. 35, pp. 1963–72.
27. R.A. Fournelle and J.B. Clark: *Metall. Trans.*, 1972, vol. 3, pp. 2757–67.
28. E.A. Brener and D.E. Temkin: *Acta Mater.*, 2003, vol. 51, pp. 797–803.
29. D. Bradai, P. Zi, E. Bischoff, and W. Gust: *Mater. Chem. Phys.*, 2003, vol. 78, pp. 222–26.
30. B. Alili, D. Bradai, and P. Zieba: *Mater. Charact.*, 2008, vol. 9, pp. 7–11.
31. Y.S. Lim, D.J. Kim, S.S. Hwang, H.P. Kim, and S.W. Kim: *Mater. Charact.*, 2014, vol. 96, pp. 28–39.
32. J. Dong, Z. Bi, N. Wang, X. Xie, Z. Wang: in *Superalloys 2008*, Champion, PA, 2008, pp. 41–50.
33. J. Radavich: in *Superalloys 718, 625, 706 Var. Deriv.*, Pittsburgh, PA, 1997, pp. 409–15.
34. X. Xie, G. Wang, J. Dong, C. Wu, J. Radavich, G. Shen, B.A. Lindsley: in *Superalloys 718, 625, 706 Var. Deriv.*, 2001, pp. 399–410.
35. T.-F. Chen, G.P. Tiwari, Y. Iijima, and K. Yamauchi: *Mater. Trans.*, 2003, vol. 44, pp. 40–46.
36. L. Karmazin: *Mater. Sci. Eng.*, 1982, vol. 54, pp. 247–56.
37. E.A. Brener and D.E. Temkin: *Acta Mater.*, 1999, vol. 47, pp. 3759–65.
38. Z. Boumerzoug and D. Hamana: *Mater. Chem. Phys.*, 2001, vol. 69, pp. 10–18.
39. M. Tařach-Dumańska, P. Zieba, A. Pawłowski, J. Wojewoda, and W. Gust: *Mater. Chem. Phys.*, 2003, vol. 80, pp. 476–81.
40. D. Duly, J.P. Simon, and Y. Brechet: *Acta Metall. Mater.*, 1995, vol. 43, pp. 101–106.
41. K.N. Tu and D. Turnbull: *Acta Metall.*, 1967, vol. 15, pp. 369–76.
42. Z. Yu, Y. Zheng, and Q. Feng: *Scr. Mater.*, 2017, vol. 128, pp. 23–26.
43. F. Findik: *J. Mater. Sci. Lett.*, 1998, vol. 7, pp. 79–83.
44. E. Clementi, D.L. Raimondi, and W.P. Reinhardt: *J. Chem. Phys.*, 1967, vol. 47, pp. 1300–07.
45. Glenn.C. Sneddon, Patrick.W. Trimby, and Julie.M. Cairney: *Mater. Sci. Eng. R Rep.*, 2016, vol. 110, pp. 1–12.
46. A.A. Gazder, A.A. Saleh, A.G. Kostryzhev, and E.V. Pereloma: *Mater. Today Proc.*, 2015, vol. 2, pp. S647–50.
47. V. Bedekar, R. Shivpuri, A. Avishai, and R. Scott Hyde: *CIRP Ann. Manuf. Technol.*, 2015, vol. 64, pp. 73–76.
48. K. Lucke and H.P. Stuwe: *Acta Metall.*, 1971, vol. 19, pp. 1087–99.
49. J.O. Andersson, T. Helander, L. Hoglund, and P.F. Shi: *Calphad*, 2002, vol. 26, pp. 273–312.
50. J.K. Chen, D. Farkas, and W.T. Reynolds, Jr: *Acta Mater.*, 1997, vol. 45, pp. 4415–21.
51. J. Cermak: *Mater. Sci. Eng. A*, 1991, vol. 148, pp. 279–87.
52. V. Rothová, J. Buršík, M. Svoboda, and J. Čermák: *Defect Diffus. Forum*, 2007, vol. 263, pp. 207–12.
53. D. Duly, M. Audier, and Y. Brechet: *Scr. Metall. Mater.*, 1993, vol. 29, pp. 1593–96.
54. David. Turnbull: *Acta Metall.*, 1955, vol. 3, pp. 55–63.
55. H.I. Aaronson and Y.C. Liu: *Scr. Metall.*, 1968, vol. 2, pp. 1–8.
56. R.W. Balluffi: *Metall. Trans. B*, 1982, vol. 13, pp. 527–53.
57. B. Verlinden, J.H. Driver, I. Samajdar, and R. D. Doherty: *Thermo-Mechanical Processing of Metallic Materials*, Pergamon Materials Series, 2007.